Quark-quark interaction and quark matter in neutron stars

Y. Yamamoto [1,*] N. Yasutake,[2] and Th. A. Rijken[3,1]
[1]*RIKEN Nishina Center, 2-1 Hirosawa, Wako, Saitama 351-0198, Japan*
[2]*Department of Physics, Chiba Institute of Technology, 2-1-1 Shibazono Narashino, Chiba 275-0023, Japan*
[3]*IMAPP, Radboud University, 6500 GL Nijmegen, The Netherlands*

(Received 2 August 2021; revised 8 November 2021; accepted 23 December 2021; published 7 January 2022)

Hyperon (Y) mixing in neutron-star matter brings about a remarkable softening of the equation of state (EoS) and the maximum mass is reduced to a value far less than $2M_\odot$. One idea to avoid this "hyperon puzzle in neutron stars" is to assume that the many-body repulsions work universally for every kind of baryons. The other is to take into account the quark deconfinement phase transitions from a hadronic EoS to a sufficiently stiff quark-matter EoS. In the present approach, both effects are handled in a common framework. As well as the hadronic matter, the quark matter with the two-body quark-quark interactions are treated within the Brueckner-Bethe-Goldstone theory beyond the mean-field frameworks, where interaction parameters are based on the terrestrial data. The derived mass-radius relations of neutron stars show that maximum masses reach over $2M_\odot$ even in the cases of including hadron-quark phase transitions, being consistent with the recent observations for maximum masses and radii of neutron stars by the Neutron Star Interior Composition Explorer (NICER) measurements and the other multimessenger data.

DOI: 10.1103/PhysRevC.105.015804

I. INTRODUCTION

In studies of neutron stars, the fundamental role is played by the equation of state (EoS) for dense nuclear matter. The observed masses of neutron stars J1614−2230 [1], J0348+0432 [2], and J0740+6620 [3] are given as $(1.97 \pm 0.04)M_\odot$, $(2.01 \pm 0.04)M_\odot$, and $(2.17^{+0.11}_{-0.10})M_\odot$, respectively, being important conditions for the stiffness of the EoS of neutron-star matter. In nonrelativistic approaches, the stiff EoS giving the maximum mass of $2M_\odot$ can be derived from the existence of strongly repulsive effects such as three-nucleon repulsions in the high-density region [4].

The hyperon (Y) mixing in neutron-star matter brings about a remarkable softening of the EoS and a maximum mass is reduced to a value far less than $2M_\odot$. The mechanism of EoS softening is understood as follows: With increasing baryon density toward centers of neutron stars, chemical potentials of neutrons become high so that neutrons at Fermi surfaces are changed to hyperons (Y) via strangeness nonconserving weak interactions overcoming rest masses of hyperons. Then, it should be noted that naively such a mechanism of EoS softening works also for mixing of any exotic particles such as quarks into neutron matter.

One of the ideas to avoid this "hyperon puzzle in neutron stars" is to assume that the many-body repulsions work universally for every kind of baryons [5]. In Refs. [6–8], the multipomeron exchange potential (MPP) was introduced as a model of universal repulsions among three and four baryons on the basis of the extended soft core (ESC) baryon-baryon interaction model developed by two of the authors (T.R. and Y.Y.) and Nagels [9].

Another solution for the hyperon puzzle has been suggested by taking into account quark deconfinement phase transitions from a hadronic-matter EoS (H-EoS) to a sufficiently stiff quark-matter EoS (Q-EoS) in the neutron-star interiors, namely by studying hybrid stars having quark matter in their cores [10–19]. It is well known that repulsive effects in quark phases are needed to result in massive neutron stars of $2M_\odot$. In the Nambu-Jona-Lasinio (NJL) model, for instance, repulsions to stiffen EoSs are given by vector interactions [20], strengths of which are treated as phenomenological parameters to stiffen the EoSs. Note that NJL models, including extended ones, are mainly based on mean-field approximations, in which two-body quark-quark interactions are not used explicitly. In spite of many works for hadron-quark phase transitions in neutron-star matter, there is not yet a unified theory of both the hadronic and quark phases.

In this work, our approach to hadron-quark phase transitions is different from the usual methods in which the deconfined quark phases are treated in mean-field approximations. We handle here the quark matter with the two-body quark-quark (QQ) potentials derived as follows: The meson-exchange quark-quark potentials are derived from the ESC baryon-baryon (BB) potentials in the framework of the constituent quark model (CQM). The quark-quark-meson (QQM) vertices are defined such that, upon folding with the Gaussian ground-state baryonic quark wave functions, the BB potentials are reproduced [21]. In this process, the QQM couplings are related to the BBM couplings, and the extra interactions at the quark level necessary to achieve this connection are completely determined. (Like in the ESC16 BB potentials, relativistic effects are included in the QQ potentials via the small

*yamamoto@tsuru.ac.jp

components of the Dirac spinors and a $1/M_Q$ expansion). The quark-quark instanton-exchange potential is derived from tuning the baryon masses (N, Λ, Σ, Ξ), and Δ_{33} in the CQM. Here, also the one-gluon exchange (OGE) and the confining potential are included.

With use of these QQ potentials together with the ESC BB potentials, baryonic matter and quark matter are treated in the common framework of the Brueckner-Bethe-Goldstone (BBG) theory, where the transitions between them are described in a reasonable way. It should be emphasized here that our QQ potentials are determined on the basis of the terrestrial data and do not include parameters only for the purpose of stiffening the quark-matter EoS.

Recently, the radius measurement has been performed for the most massive neutron star PSR J0740+6620: The two analyses have been done independently for the x-ray data taken by the Neutron Star Interior Composition Explorer (NICER) and the X-ray Multi-Mirror (XMM-Newton) observatory. The radius and mass are $12.39^{+1.30}_{-0.98}$ km and $2.072^{+0.067}_{-0.066}$ $M_\odot$ [22] or $13.7^{+2.6}_{-1.5}$ km (68%) and 2.08 ± 0.07 $M_\odot$ [23]. The radius of a typical $1.4M_\odot$ neutron star $R_{1.4M_\odot}$ has been estimated by combining the NICER measurements and the other multimessenger data [24,25]. In Ref. [24], the two values of $R_{1.4M_\odot} = 12.33^{+0.76}_{-0.81}$ km and $R_{1.4M_\odot} = 12.18^{+0.56}_{-0.79}$ km are obtained for the two different high-density EoSs of a piecewise-polytrophic (PP) model and a model based on the speed of sound, respectively. In Ref. [25], the estimated value is $R_{1.4M_\odot} = 11.94^{+0.76}_{-0.87}$ km at 90% confidence. These values of radii are rather similar to each other. On the other hand, when the implication of PREX-II for the neutron skin thickness of heavy nuclei are taken into account on the neutron-star EoS, they obtain 13.33 km $< R_{1.4M_\odot} <$ 14.26 km [26]. Our obtained EoSs in this work are investigated in the light of these new data.

This paper is organized as follows: In Sec. II, the hadronic-matter EoS (H-EoS) is recapitulated on the basis of our previous works. In Sec. III, on the basis of realistic QQ interaction models, the BBG theory is applied to quark matter: In Sec. III A, the G-matrix framework is outlined for quark matter. In Sec. III B, our QQ potentials are explained, which are composed of the extended meson-exchange potential, the multipomeron potential, the instanton potential, and the one-gluon exchange potential. In Sec. III C, the QQ G-matrix interactions in coordinate space are parameterized as density-dependent interactions. In Sec. IV, there are obtained the quark-matter EoSs (Q-EoS) and mass-radius (MR) diagrams of hybrid stars: In Sec. IV A, Q-EoSs are derived. In Sec. IV B, hadron-quark phase transitions in hybrid stars are investigated on the basis of the obtained EoSs. In Sec. IV C, the MR relations of hybrid stars are obtained by solving the TOV equation. The conclusion of this paper is given in Sec. V.

II. HADRONIC-MATTER EOS

HERE, THE hadronic matter is defined exactly as β-stable baryonic matter including leptons. On the basis of the BBG theory, the hadronic-matter EoS (H-EoS) is derived with use of the ESC baryon-baryon interaction model [6–8]. Then, the EoS is stiff enough to assure the neutron-star masses of $2M_\odot$, if the strong three-nucleon repulsion is taken into account. However, the hyperon (Y) mixing results in remarkable softening of the EoS canceling this repulsive effect. In order to avoid this "hyperon puzzle," it is assumed that the repulsions work universally for YNN, YYN, YYY, as well as for NNN. In Refs. [6–8], such universal repulsions are modeled as the multipomeron exchange potential (MPP). In Ref. [8], they proposed three versions of MPP: MPa, MPa$^+$, and MPb. MPa and MPa$^+$ (MPb) include the three- and four-body (only three-body) MPPs, where mixings of Λ and Σ^- hyperons are taken into account. The three-body part of MPa (MPa$^+$) is less repulsive than (equal to) that of MPb, and the four-body parts of MPa and MPa$^+$ are equal to each other. The EoSs for MPa and MPa$^+$ are stiffer than that for MPb, because of which radii of neutron stars obtained from the formers are larger than those from the latter. Our ESC BB interactions including MPb, MPa, and MPa$^+$ are named as H1, H2, and H3, for simplicity. In addition, we introduce two versions, H0 and H1′, for comparative studies: H0 is the nucleon-nucleon part of H1, being used in nuclear-matter EoSs with no hyperons. H1′ is the BB interaction H1 in which MPP works only among nucleons. In the case of H1′, the remarkable softening of the EoS is brought about by hyperon mixing.

As shown later, neutron-star radii R for masses lower than about $1.5M_\odot$ are determined by H-EoSs even in our MR diagrams including hadron-quark transitions. For the H-EoSs derived from the above BB interactions, the obtained values of radii at $1.4M_\odot$ ($R_{1.4M_\odot}$) are 12.4 km (H1), 13.3 km (H2), and 13.6 km (H3).

III. QUARK-QUARK INTERACTION AND QUARK MATTER

A. G-matrix framework

The BBG theory is adopted for studies of quark matter on the basis of two-body QQ potentials given in Ref. [21]. Here, correlations induced by QQ potentials are renormalized into coordinate-space G-matrix interactions, being considered as effective QQ interactions to derive the Q-EoS. In this stage to construct G-matrix interactions in quark matter, color quantum numbers are not taken into account.

We start from the G-matrix equation for the quark pair $f_1 f_2$ in quark matter, where f_1 and f_2 denote flavor quantum numbers (u, d, s):

$$G_{cc_0} = v_{cc_0} + \sum_{c'} v_{cc'} \frac{Q_{y'}}{\omega - \epsilon_{f_1'} - \epsilon_{f_2'}} G_{c'c_0}, \tag{3.1}$$

where c denotes a relative state (y, T, L, S, J) with $y = f_1 f_2$, and S and T being spin and isospin quantum numbers, respectively. Orbital and total angular momenta are denoted by L and J, respectively, with $\mathbf{J} = \mathbf{L} + \mathbf{S}$: A two-quark state is specified by ${}^{2S+1}L_J$. In Eq. (3.1), ω gives the starting energy in the starting channel c_0. The Pauli operator Q_y acts on intermediate quark states with $y = f_1 f_2$. We adopt for simplicity the gap choice for the intermediate states in the G-matrix equation, meaning that an intermediate energy ϵ_f is replaced by a kinetic-energy operator. The G-matrix Eq. (3.1) is represented

in the coordinate space, whose solutions give rise to G-matrix elements.

The quark single particle (s.p.) energy ϵ_f in quark matter is given by

$$\epsilon_f(k_f) = \frac{\hbar^2 k_f^2}{2m_f} + U_f(k_f) \tag{3.2}$$

where k_f is an f-quark momentum ($f = u, d, s$). The potential energy U_f is obtained self-consistently in terms of the G matrix as

$$U_f(k_f) = \sum_{|\mathbf{k}_{f'}|} \langle \mathbf{k}_f \mathbf{k}_{f'} | G_{ff'}(\omega = \epsilon_f(k_f) + \epsilon_{f'}(k_{f'})) | \mathbf{k}_f \mathbf{k}_{f'} \rangle, \tag{3.3}$$

where $(TLSJ)$ quantum numbers are implicit. Then, the potential energy per particle $\langle U \rangle = \sum_f \langle U_f \rangle$ is obtained by averaging $U_f(k_f)$ over f:

$$\langle U \rangle = \frac{3}{2} \sum_f \omega_f \int_0^{k_F^f} \frac{d^3 k_f}{(2\pi)^3} U_f(k_f) \tag{3.4}$$

where $\omega_f = \rho_f / (\sum_{f'} \rho_{f'})$ with an f-quark density ρ_f. Making a partial wave reduction of Eq. (3.3) with explicit use of $TLSJ$ quantum numbers, $U_f(k_f)$ is represented as a sum of $U_f^{TLSJ}(k_f)$ obtained from G-matrix elements $G_{ff'}^{TLSJ}$.

B. Quark-quark interactions

Our QQ interaction is given by

$$V_{QQ} = V_{\rm EME} + V_{\rm INS} + V_{\rm OGE} + V_{\rm MPP} \tag{3.5}$$

where $V_{\rm EME}$, $V_{\rm INS}$, $V_{\rm OGE}$, and $V_{\rm MPP}$ are the extended meson-exchange potential, the instanton exchange potential, the one-gluon exchange potential, and the multipomeron potential, respectively [21]. The included parameters in our QQ potential are chosen so as to be consistent with physical observables as much as possible. The contributions of the confining potential ($V_{\rm conf}$) to V_{QQ} are minor in quark matter, being omitted in this work.

The $V_{\rm EME}$ QQ potential is derived from the ESC16 BB potential [9] so that the QQM couplings are related to the BBM couplings through folding procedures with Gaussian baryonic quark wave functions. Then, the $V_{\rm EME}$ QQ potential is basically of the same functional expression as the ESC16 BB potential. The explicit expressions for $V_{\rm EME}$ QQ potentials are given in Ref. [21]. In the ESC modeling, the strongly repulsive components in BB potentials are described mainly by vector-meson and pomeron exchanges between baryons. It should be noted that this feature persists in the $V_{\rm EME}$ QQ potential, which includes the strongly repulsive components originated from vector-meson and pomeron exchanges between quarks.

Multipomeron exchanges are expected to work not only among baryons but also among quarks, in which the baryon mass M_B is replaced by the quark mass $M_Q = M_B/3$ and the pomeron-baryon-baryon coupling constant g_{PBB} is replaced by the pomeron-quark-quark coupling constant g_{PQQ}. In this work, the QQ multipomeron potential $V_{\rm MPP}$ is derived from the version MPa for the MPP among baryons.

The included parameters included in $V_{\rm INS}$ and $V_{\rm OGE}$ are chosen so as to reproduce basic features of baryon mass spectra. The form of the one-gluon exchange potential is given as

$$V_{\rm OGE}(r) = \tfrac{1}{4} \left(\lambda_{\mathbf{1}}^{\mathbf{C}} \cdot \lambda_{\mathbf{2}}^{\mathbf{C}} \right) \alpha_S \, V_{\rm vector}(m_G; r) \tag{3.6}$$

where λ_a^C, $a = 1 \ldots 8$ are the Gell-Mann matrices in color SU(3) space and $V_{\rm vector}(m_G; r)$ is the vector-type one boson exchange potential. Its explicit form is given by Eq. (E9a) in Ref. [21]. The strength of $V_{\rm OGE}$ is determined by the quark-gluon coupling constant α_S, being fixed as $\alpha_S = 0.25$ in this work. The gluon mass m_G is taken as 420 MeV [27]. In quark matter, $(\lambda_{\mathbf{1}}^{\mathbf{C}} \cdot \lambda_{\mathbf{2}}^{\mathbf{C}}) = -8/3, +4/3, +4/3, -8/3$ in states of $(S, T) = (0, 0), (0, 1), (1, 0), (1, 1)$, respectively.

The instanton potential $V_{\rm INS}$ is based on the SU(3) generalization of the 't Hooft interaction for (u, d, s) quarks. In the configuration space, with the addition of the Gaussian cutoff $\exp(-k^2/\Lambda_I^2)$, the local instanton potential is given as [21]

$$\begin{aligned} V_{\rm INS}(r) = & -\left(4/3 - \boldsymbol{\lambda}_{\mathbf{1}}^{\boldsymbol{F}} \cdot \boldsymbol{\lambda}_{\mathbf{2}}^{\boldsymbol{F}}\right) G_I \left(\frac{\Lambda_I}{2\sqrt{\pi}} \right)^3 \\ & \times \left[1 + \frac{\Lambda_I^2}{2m_Q^2} \left(3 - \frac{1}{2}\Lambda_I^2 r^2 \right) \left(1 - \frac{1}{3} \boldsymbol{\sigma_1} \cdot \boldsymbol{\sigma_2} \right) \right] \\ & \times \exp\left(-\frac{1}{4}\Lambda_I^2 r^2 \right), \end{aligned} \tag{3.7}$$

where λ_a^F, $a = 1 \ldots 8$ are the Gell-Mann matrices in flavor SU(3) space and m_Q is the quark mass. In two-quark states, λ^F operators are reduced to τ operators of isospin. The strength of $V_{\rm INS}$ is determined by coupling constant G_I and cutoff mass Λ_I. They are taken as $G_I = 2.5$ GeV^{-2} and $\Lambda_I = 0.55$ GeV, being estimated from the $\pi - \rho$ mass splitting.

In order to demonstrate the features of our QQ interaction, we show the averaged s.p. potentials $\langle U \rangle$ given by Eq. (3.4) as a function of the baryon number density $\rho_B = \frac{1}{3}\rho_Q$ in the case of $\rho_u = \rho_d = \rho_s$. In Fig. 1, the solid, short-dashed, long-dashed, and dot-dashed curves are the contributions to $\langle U \rangle$ from $V_{\rm EME}$, $V_{\rm MPP}$, $V_{\rm OGE}$, and $V_{\rm INS}$, respectively. The bold solid curve is obtained by the sum of $V_{\rm EME} + V_{\rm MPP} + V_{\rm INS} + V_{\rm OGE}$. The strongly repulsive nature of $\langle U(\rho_B) \rangle$ is the key point in this work, which leads to the quark-matter EoS stiff enough to reproduce neutron-star masses over $2M_\odot$. In the figure, the repulsive contribution of $V_{\rm EME}$ is found to be essential the repulsive nature of $\langle U(\rho_B) \rangle$, where the repulsive contributions of $V_{\rm OGE}$ and $V_{\rm MPP}$ are considerably canceled by the attractive contribution of $V_{\rm INS}$. It is worthwhile to say that the repulsive components in $V_{\rm EME}$ are from the vector-meson and pomeron exchanges. This feature persists from the ESC BB interaction model.

In neutron matter, $\langle U \rangle$ includes repulsive contributions from the multipomeron potential MPP, being quite large in high density regions. The strengths of three- and four-body parts of MPP are proportional to $(g_{PBB})^3$ and $(g_{PBB})^4$, respectively, g_{PBB} being the pomeron-baryon-baryon coupling constant. In QQ potentials, g_{PBB} is replaced by the pomeron-quark-quark coupling constant g_{PQQ}. Because of the relation $g_{PQQ} = \frac{1}{3} g_{PBB}$, the strengths of three- and four-body parts of MPP among quarks are far smaller than those among baryons.

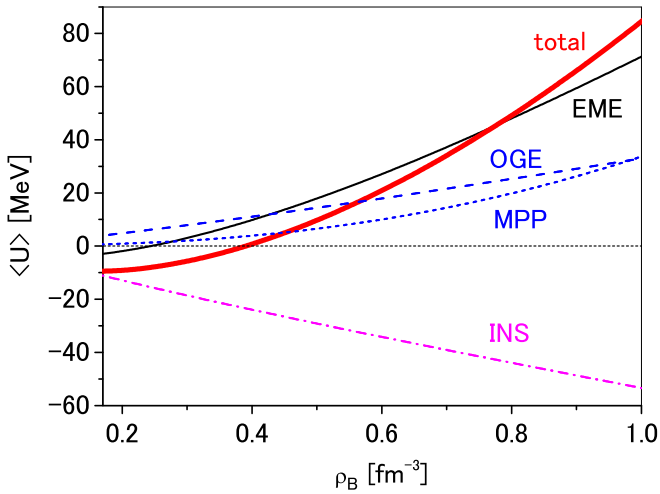

FIG. 1. Averaged single particle potentials $\langle U\rangle$ in quark matter as a function of the baryon number density $\rho_B = \frac{1}{3}\rho_Q$ in the case of $\rho_u = \rho_d = \rho_s$. The solid, short-dashed, long-dashed, and dot-dashed curves are the contributions to $\langle U\rangle$ from $V_{\rm EME}$, $V_{\rm MPP}$, $V_{\rm OGE}$, and $V_{\rm INS}$, respectively. The bold solid curve is obtained by $V_{\rm EME} + V_{\rm MPP} + V_{\rm INS} + V_{\rm OGE}$.

Therefore, MPPs among quarks are not so remarkable in comparison with those among baryons.

The even- and odd-state contributions to $\langle U\rangle$ are denoted as $\langle U_{\rm even}\rangle$ and $\langle U_{\rm odd}\rangle$, respectively. In Fig. 2, the solid curve shows $\langle U(\rho_B)\rangle$ obtained from $V_{\rm EME}$, and $\langle U_{\rm even}(\rho_B)\rangle$ and $\langle U_{\rm odd}(\rho_B)\rangle$ are given by the dashed and short-dashed curves. The dotted curves are the even- and odd-state contributions of averaged neutron potentials $\langle U_{\rm even}\rangle$ and $\langle U_{\rm odd}\rangle$ in neutron matter. The remarkable feature of $\langle U_{\rm even}\rangle$ and $\langle U_{\rm odd}\rangle$ given by $V_{\rm EME}$ is that they are attractive and repulsive, respectively.

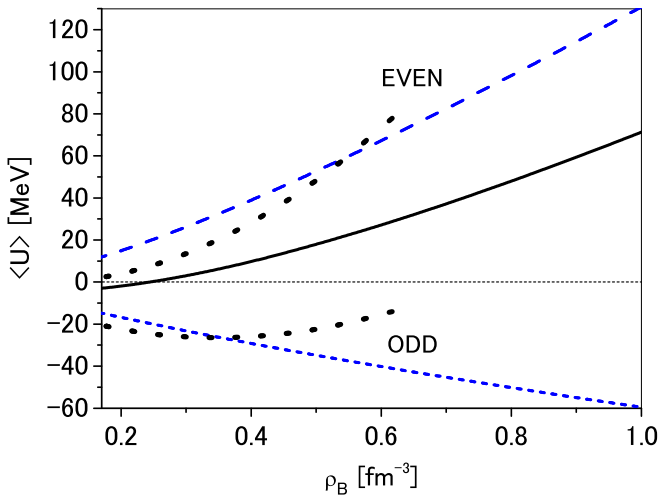

FIG. 2. Averaged single particle potentials $\langle U\rangle$ in quark matter as a function of the baryon number density $\rho_B = \frac{1}{3}\rho_Q$ in the case of $\rho_u = \rho_d = \rho_s$. The solid curve is obtained from $V_{\rm EME}$. The even- and odd-state contributions $\langle U_{\rm even}\rangle$ and $\langle U_{\rm odd}\rangle$ are given by the dashed and short-dashed curves. The dotted curves are the corresponding values of $\langle U_{\rm even}\rangle$ and $\langle U_{\rm odd}\rangle$ in neutron matter.

This feature of $\langle U_{\rm even}\rangle$ and $\langle U_{\rm odd}\rangle$ is similar to the corresponding one in neutron matter qualitatively.

When our QQ potentials are used in quark-matter calculations, it is reasonable to assume the constituent quark masses originated from the chiral symmetry breaking as the QCD nonperturbative effect. Then, it is probable that the constituent quark masses in quark matter become smaller than those in vacuum and move to current masses in the high-density limit. At the mean-field (MF) level, usually the density-dependent quark masses in matter have been derived from the MF-Lagrangian such as that of the NJL model. In the present approach, we introduce phenomenologically the density-dependent quark mass

$$M_Q^*(\rho_Q) = M_0/[1 + \exp\{\gamma(\rho_Q - \rho_c\}] + m_0 + C \quad (3.8)$$

with $C = M_0 - M_0/[1 + \exp(-\gamma\rho_c)]$ assuring $M_Q^*(0) = M_0 + m_0$, where ρ_Q is number density of quark matter, and M_0 and m_0 are taken as 300 (360) MeV and 5 (140) MeV for u and d (s) quarks. Then, we have $M_Q^*(0) = 305$ (500) MeV for u and d (s) quarks. The adjustable parameters ρ_c and γ are used to control mainly the onset densities of quark phases into hadronic phases.

Furthermore, because the quark mass reduction has to bring about an increase of the vacuum energy B, we assume simply

$$B(\rho_Q) = M_Q^*(0) - M_Q^*(\rho_Q). \quad (3.9)$$

It is well known that there are three schemes for the density-dependent quark mass [28]: (i) a constant quark mass, (ii) a linear density dependence (Brown-Rho scaling [29]), and (iii) a density dependence within a higher order NJL model [30,31]. Equation (3.8) includes these schemes, representing (i) for $\gamma = 0$, (ii) for small values of γ, and (iii) for large values of γ. The parameter ρ_c is chosen as $6\rho_0$ by referring to forms of (iii) derived from the higher order NJL models.

We define the following five sets with different values of γ of QQ interactions for deriving Q-EoSs.

Q0 : $V_{\rm EME}$ with γ=1.2,

Q1 (Q1e) : $V_{\rm EME} + V_{\rm INS} + V_{\rm OGE}$ with $\gamma = 1.0$ ($\gamma = 2.6$),

Q2 (Q2e) : $V_{\rm EME} + V_{\rm MPP} + V_{\rm INS} + V_{\rm OGE}$ with $\gamma = 1.6$ ($\gamma = 2.2$).

In the cases of Q0, Q1, and Q2, the values of γ are chosen so that the critical chemical potentials and densities for phase transitions are as small as possible. In the cases of Q1e and Q2e, they are chosen so that critical densities are near crossing points of hadronic and quark energy densities.

In Fig. 3, the quark mass $M_Q^*(\rho_Q)$ ($Q = u, d$) as a function of the baryon number density $\rho_B = \rho_Q/3$ is plotted in the cases of (a) Q1, (b) Q1e, (c) Q2, and (d) Q2e. The density-dependent quark masses in these cases (especially Q1e and Q2e) are found to be rather close to (ii) with the Brown-Rho scaling.

It is quite important to use the density-dependent quark masses together with our QQ potentials. When constant quark masses are used, hadron-quark transitions derived from our QQ potentials occur in density regions over $5\rho_0$ in hadronic matter giving $2M_\odot$ masses. In such a case, quark phases have

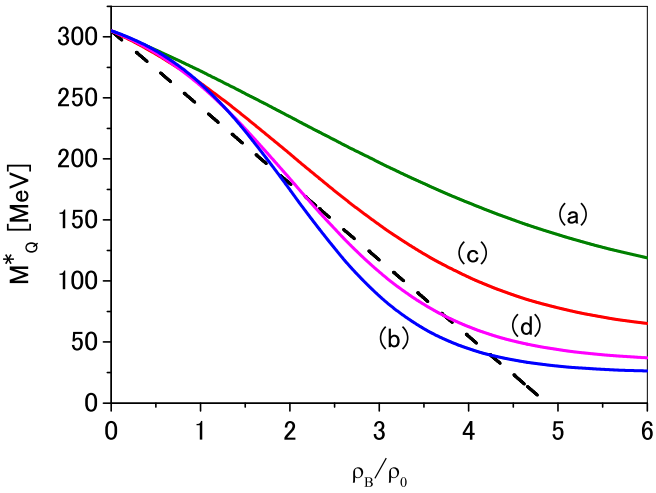

FIG. 3. Quark mass as a function of the baryon number density ρ_B for the (a) Q1, (b) Q1e, (c) Q2, and (d) Q2e models. As a reference, also the Brown-Rho scaling is shown by the dashed line.

no effect on masses and radii of neutron stars, even if they exist in inner cores.

For instance, when the baryon-baryon interaction H2 is used together with quark-quark interaction Q2, the combined set is denoted as H2+Q2. Hereafter, combinations of *BB* and *QQ* interactions are expressed like this.

C. Effective quark-quark interactions

For applications to quark-matter calculations, we construct density-dependent effective local interactions $\mathcal{G}_{QQ}(\rho_Q; r)$ simulating G matrices in coordinate space, where ρ_Q is number density of quark matter. We use here the method given in Ref. [32].

The effective interactions are written as $\mathcal{G}_{QQ} = \mathcal{G}_{\rm EME} + \mathcal{G}_{\rm MPP} + \mathcal{G}_{\rm INS} + \mathcal{G}_{\rm OGE}$ approximately corresponding to $V_{QQ} = V_{\rm EME} + V_{\rm MPP} + V_{\rm INS} + V_{OGE}$. Though they can be obtained for each (ff', T, L, S, J) state, for simplicity, the dependence on L is approximated by that on parity P and the dependence on J is averaged: Quantum numbers $TLSJ$ are reduced to TSP. The respective interactions are represented in two- or one-range Gaussian forms, and coefficients are adjusted so that s.p. potentials U_f^{TSP} obtained from $\mathcal{G}_{ff'}^{TSP}$ simulate the original G-matrix results. It is far easier to derive quark-matter EoSs with use of these density-dependent interactions $\mathcal{G}_{QQ}$ than derivations by G-matrix calculations with V_{QQ}.

The density-dependent effective interactions $\mathcal{G}_{\rm EME}$ and $\mathcal{G}_{\rm OGE}$ derived from $V_{\rm EME}$ and $V_{\rm OGE}$, respectively, are parameterized in a two-range Gaussian form as

$$\mathcal{G}_{\rm EME,OGE}(\rho, r) = (a\rho^\alpha + b\rho^\beta)\exp[-(r/0.8)^2] + c\exp[-(r/1.6)^2]. \quad (3.10)$$

The parameter set (a, α, b, β, c) in Eq. (3.10) is given for each (y, T, S, P) state with $y = qq, qs, ss$ $(q = u, d)$. In Tables I and II, the values of parameters are tabulated for $\mathcal{G}_{\rm EME}$ and $\mathcal{G}_{\rm OGE}$, respectively.

TABLE I. $\mathcal{G}_{\rm EME}(\rho, r) = (a\rho^\alpha + b\rho^\beta)\cdot\exp[-(r/0.8)^2] + c\cdot\exp[-(r/1.6)^2]$. $y = qq, qs, ss$ $(q = u, d)$.

y	T S P	a	α	b	β	c
qq	1 0 +	−3.520	−1	−17.94	0	−0.9978
	0 1 +	−2.871	−1	−30.59	0	−0.8389
	0 0 −	43.34	−1	192.8	0	3.896
	1 1 −	6.621	−1	102.5	0	1.595
qs	1/2 0 +	−0.5716	−1	−28.27	0	−0.4530
	1/2 1 +	−0.6959	−1	−24.58	0	−0.1993
	1/2 0 −	−1.597	−1	149.0	0	1.568
	1/2 1 −	1.183	−1	75.98	0	1.217
ss	0 0 +	−2.755	−1	−26.37	0	−0.1212
	0 1 −	−1.651	−1	51.06	0	0.3558

$\mathcal{G}_{\rm INS}$ derived from $V_{\rm INS}$ is parameterized in an one-range Gaussian form as

$$\mathcal{G}_{\rm INS}(\rho, r) = (a\rho^\alpha + b\rho^\beta)\exp[-(r/0.6)^2]. \quad (3.11)$$

The parameter set (a, α, b, β, c) in Eq. (3.11) is given for each (y, T, S, P) state with $y = qq, qs$ $(q = u, d)$. The values of them are given in Table III.

$\mathcal{G}_{\rm MPP}$ derived from $V_{\rm MPP}$ is parameterized in an one-range Gaussian form as

$$\mathcal{G}_{\rm MPP}(\rho, r) = (a + b\rho^\beta)\exp[-(r/1.3)^2] \quad (3.12)$$

being independent of (y, T, S) and given only for P. The values of parameters (a, b, β) are given in Table IV.

IV. EOS AND *MR* DIAGRAM OF HYBRID STAR

A. Derivation of quark-matter EoS

Let us derive the EoS of quark matter composed of quarks with flavor $f = u, d, s$. In this derivation, we use the density-dependent QQ interactions Eqs. (3.10)–(3.12) based on the nonrelativistic formalism. Relativistic expressions are used only for kinetic energies.

TABLE II. $\mathcal{G}_{\rm OGE}(\rho, r) = (a\rho^\alpha + b\rho^\beta)\cdot\exp[-(r/0.8)^2] + c\cdot\exp[-(r/1.6)^2]$. $y = qq, qs, ss$ $(q = u, d)$.

y	T S P	a	α	b	β	c
qq	1 0 +	8.565	1	3.892	0.3742	0.5185
	0 1 +	7.543	1	1.977	0.6431	1.142
	0 0 −	−0.8959	1	9.982	0.2741	0.5027
	1 1 −	8.094	1	11.64	0.2881	1.147
qs	1/2 0 +	−4.733	1	−1.359	0.4161	−0.2593
	1/2 1 +	−3.658	1	−0.7316	0.6347	−0.5709
	1/2 0 −	−1.282	1	−3.141	0.3675	−0.2514
	1/2 1 −	−5.645	1	−3.831	0.3727	−0.5736
ss	0 0 +	10.48	1	1.478	0.5930	0.5185
	0 1 −	11.23	1	7.743	0.3250	1.147

TABLE III. $\mathcal{G}_{\rm INS}(\rho, r) = (a\rho^\alpha + b\rho^\beta)\cdot\exp[-(r/0.6)^2]$. $y = qq, qs$ $(q = u, d)$.

y	$T\ S\ P$	a	α	b	β
qq	0 1 +	0.2132	−1	−130.0	0
	0 0 −	124.8	0	−38.82	0.4227
qs	1/2 0 +	−1.504	−1	−61.35	0.0705
	1/2 1 +	−0.1638	−1	−63.47	0
	1/2 0 −	59.03	0	−17.06	0.4966
	1/2 1 −	−36.95	0	−5.749	0.3192

A single f quark potential in quark matter composed of f' quarks is given by

$$U_f(k) = \sum_{f'} U_f^{(f')}(k) = \sum_{f'}\sum_{k'<k_F^{f'}} \langle kk'|\mathcal{G}_{ff',ff'}|kk'\rangle \quad (4.1)$$

with $f, f' = u, d, s$, where spin and isospin quantum numbers are implicit. The quark energy density is given by

$$\varepsilon_f = 2N_c \sum_f \int_0^{k_F^f} \frac{d^3k}{(2\pi)^3}\left\{\sqrt{\hbar^2k^2 + M_f^2} + \frac{1}{2}U_f(k)\right\} + B(\rho_Q), \quad (4.2)$$

where $N_c = 3$ is the number of quark colors. The quark number density is given as $\rho_Q = \sum_f \rho_f$ with $\rho_f = N_c\frac{(k_F^f)^3}{3\pi^2}$. The chemical potential μ_f and pressure P_Q are expressed as

$$\mu_f = \frac{\partial\varepsilon_Q}{\partial\rho_f}, \quad (4.3)$$

$$P_Q = \rho_Q^2\frac{\partial(\varepsilon_Q/\rho_Q)}{\partial\rho_Q} = \sum_f \mu_f\rho_f - \varepsilon_Q. \quad (4.4)$$

Here, we consider the EoS of β-stable quark matter composed of u, d, s, e^-. The equilibrium conditions are summarized as follows:

(1) chemical equilibrium conditions

$$\mu_d = \mu_s = \mu_u + \mu_e, \quad (4.5)$$

(2) charge neutrality

$$0 = \tfrac{1}{3}(2\rho_u - \rho_d - \rho_s) - \rho_e, \quad (4.6)$$

(3) baryon number conservation

$$\rho_B = \tfrac{1}{3}(\rho_u + \rho_d + \rho_s) = \tfrac{1}{3}\rho_Q. \quad (4.7)$$

In the parabolic approximation, the following relation can be derived:

$$\mu_e = \mu_d - \mu_u = 4\beta E_{\rm sym}, \quad (4.8)$$

where $x = \rho_u/(\rho_u + \rho_d)$ and $\beta = 1 - 2x$. $E_{\rm sym}$ is the symmetric energy of ud part.

TABLE IV. $\mathcal{G}_{MPP}(\rho, r) = (a + b\rho^\beta)\cdot\exp(-(r/1.3)^2)$.

P	a	b	β
+	0.3597	1.600	1.490
−	0.4338	2.618	1.384

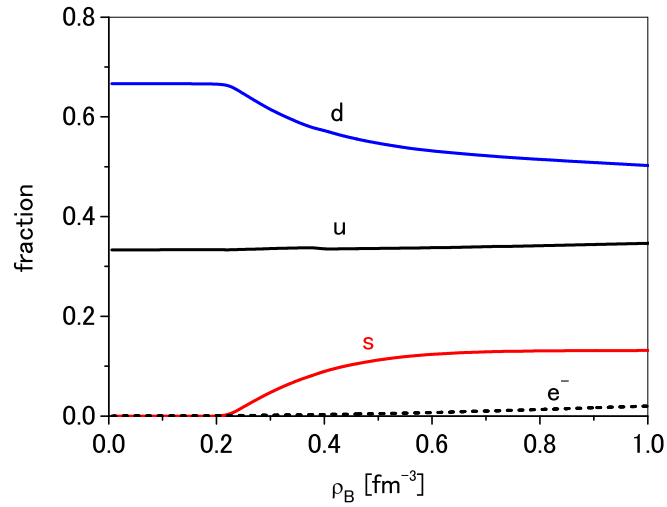

FIG. 4. The number fractions of quarks and electrons in β-stable quark matter as a function of the baryon density ρ_B in the case of using Q2. The fractions of u, d, and s quarks are given by solid curves, and that of electrons e^- are by dashed curve.

When the chemical potentials (4.3) are substituted into (4.5), the chemical equilibrium conditions are represented as equations for densities ρ_u, ρ_d, ρ_s, and ρ_e. Then, Eqs. (4.5)–(4.7) are solved iteratively, and densities and chemical potentials in equilibrium are obtained. Finally, energy densities (4.2) and pressures (4.4) can be calculated.

An example of solution is demonstrated in Fig. 4: The number fractions of quarks and electrons in β-stable quark matter are plotted as a function of the baryon density ρ_B in the case of using Q2, where solid (dashed) curves are for u, d, and s quarks (electrons). In the figure, the electron fractions are not visible below the s-quark onset. The reason of such small values are because the symmetry energies $E_{\rm sym}$ in Eq. (4.8) are not so large in the case of our QQ interactions.

B. Phase transition from hadronic matter to quark matter

The EoSs are shown in Fig. 5, where pressures of quark matter are given as a function of the energy density ϵ and compared to those of hadronic matter. Steeper slopes of curves correspond to stiffer EoSs: The Q-EoSs are stiffer than the H-EoSs, and the EoSs for [Fig. 5(b)] Q1 and [Fig. 5(c)] Q2 are stiffer than that for [Fig. 5(a)] Q0 owing to the repulsive contributions of $V_{\rm OGE}$ and $V_{\rm MPP}$. As shown later, these features are clearly reflected in the MR curves of hybrid stars.

In order to construct the hybrid EoS including a transition from hadronic phase and quark phase, we use the replacement interpolation method [14,33], being a simple modification of the Maxwell and the Glendenning (Gibbs) constructions [34]. In our actual calculations, we follow the interpolation formula given in Ref. [14]. Then, interpolated regions can be considered as mixed phases. Both of H-EoSs and Q-EoSs are assumed to fulfill separately the charge-neutrality and β-equilibrium conditions. The EoSs of hadronic and quark phases and that of mixed phase are described with the relations between pressures and chemical potentials $P_H(\mu)$,

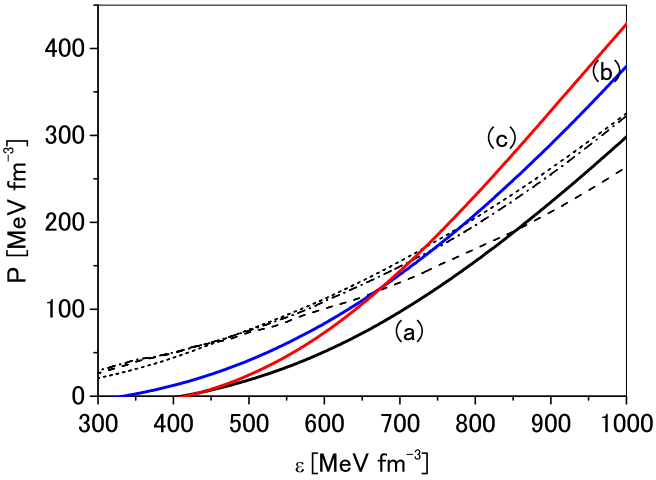

FIG. 5. Pressures of hadronic matter and quark matter as a function of the energy density ϵ. Short-dashed, long-dashed, and dot-dashed curves are for hadronic matter for H1, H2, and H3, respectively. Solid curves are for quark matter obtained from (a) Q0, (b) Q1, and (c) Q2.

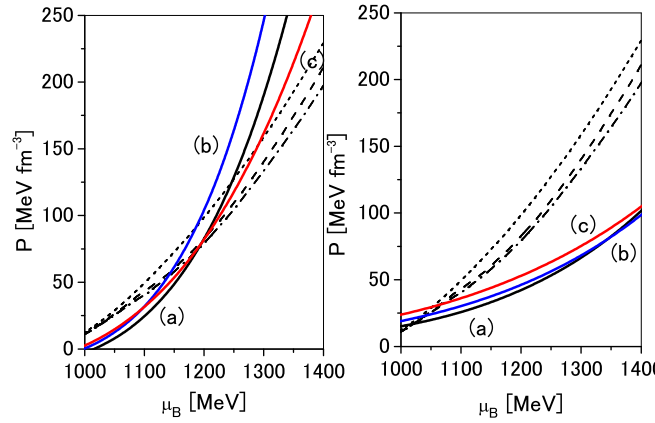

FIG. 6. Pressures as a function of the chemical potential μ_B. Short-dashed, long-dashed, and dot-dashed curves are pressures of hadronic matter for H1, H2, and H3, respectively. In the left panel, solid curves are pressures of quark matter obtained from (a) Q0, (b) Q1, and (c) Q2. In the right panel, they are obtained by using constant quark masses without density dependences Eq. (3.8) and vacuum energies Eq. (3.9).

$P_Q(\mu)$, and $P_M(\mu)$, respectively. The critical chemical potential μ_c for the transition from the hadronic phase to the quark phase is obtained from the Maxwell condition

$$P_Q(\mu_c) = P_H(\mu_c) = P_c. \tag{4.9}$$

The pressure of the mixed phase is represented by a polynomial ansatz

$$P_M(\mu) = \sum_{q=1}^{N} \alpha_q (\mu - \mu_c)^q + P_c + \Delta P, \tag{4.10}$$

where the pressure shift ΔP at μ_c is treated as a free parameter. The pressure of the mixed phase at μ_c is determined by $P_M(\mu_c) = P_c + \Delta P = (1 + \Delta_P)P_c$ with $\Delta_P = \Delta P/P_c$. Then, the matching chemical potential μ_H (μ_Q) of $P_M(\mu)$ to $P_H(\mu)$ [$P_Q(\mu)$] can be obtained from the continuity condition. The corresponding matching densities ρ_H and ρ_Q are obtained with use of $\rho(\mu) = dP(\mu)/d\mu$. The finite values of $\Delta_P =$ 0.05–0.07 corresponds to the Glendenning construction [14]. We choose $\Delta_P = 0.07$ in this work.

In Fig. 6, pressures are drawn as a function of the chemical potential μ_B, where short-dashed, long-dashed, and dot-dashed curves are pressures of hadronic matter for H1, H2, and H3, respectively. In the left panel, solid curves are pressures of quark matter obtained from (a) Q0, (b) Q1, and (c) Q2. The crossing of the hadronic and the quark-matter curves is considered to be a condition for phase transition to occur. The values of P at crossing points give the critical pressures P_c for phase transitions. The hadronic and quark-matter curves are connected smoothly by Eq. (4.10). Then, the effective-mass parameter γ in Eq. (3.8) is adjusted so that cross points appear at similar values of $\mu_B \approx 1200$ MeV. In the right panel, on the other hand, solid curves are obtained from Q0, Q1, and Q2 by using constant quark masses $M_Q^*(\rho_Q = 0)$ without density dependences Eq. (3.8) and vacuum energies Eq. (3.9). It is found that there is no crossing point in this region of μ_B. Thus, the density-dependent quark mass plays a decisive role in the occurrence of phase transition.

In Fig. 7, pressures are given as a function of the chemical potential μ_B in the transition region. The short-dashed curve is obtained by the H-EoS for H2 and the solid curve is by the Q-EoS for Q2. The bold solid curve is obtained by the interpolation method.

Our phase transition is specified by the pressures P_c at critical chemical potentials μ_c and boundary values of chemical potentials and densities for mixed phases. They are shown in the cases of phase transitions from the H-EoS for H1, H2, and H3 to the Q-EoSs for Q0, Q1, Q2, Q1e, and Q2e. In Table V, the chemical potentials at matching points are given by values of μ_H and μ_Q. In Table VI, ρ_H and ρ_Q are densities

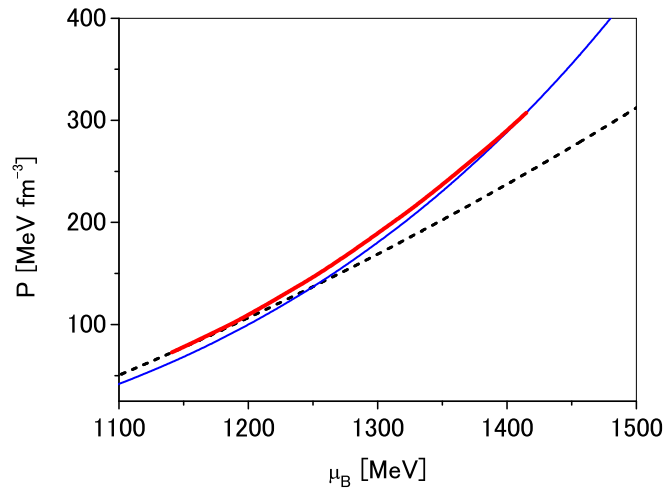

FIG. 7. Pressures as a function of the chemical potential μ_B in the transition region. The short-dashed curve is obtained by the H-EoS for H2 and the solid curve is by the Q-EoS for Q2. The bold solid curve is the interpolated one.

TABLE V. Pressures P_c at critical chemical potentials μ_c in phase transitions from the hadronic phases for H1, H2, and H3 to the quark-matter phases for Q0, Q1, and Q2. Values of μ_H (μ_Q) are chemical potentials at matching points between mixed phases and hadron (quark) phases.

	P_c (MeV/fm^3)	μ_c (MeV)	μ_H (MeV)	μ_Q (MeV)
H1+Q0	125.7	1241	1186	1373
H1+Q1	92.55	1183	1141	1277
H1+Q2	110.4	1215	1095	1368
H2+Q0	139.6	1254	1199	1386
H2+Q1	102.3	1193	1149	1282
H2+Q2	138.2	1252	1141	1415
H2+Q1e	132.9	1189	1243	1446
H2+Q2e	209.6	1360	1261	1600
H3+Q0	136.0	1251	1198	1382
H3+Q1	101.2	1191	1148	1279
H3+Q2	131.6	1243	1142	1412

at matching points in phase transitions, and ρ_H^c and ρ_Q^c are critical densities defined by the $P_H(\rho_H^c) = P_Q(\rho_Q^c) = P_c$ in the case of $\Delta_P = 0$. It is reasonable that that the values of ρ_H^c and ρ_Q^c are between the values of ρ_H and ρ_Q. The Maxwell construction is conditioned by $\rho_H^c < \rho_Q^c$. As found in Table VI, however, the values of ρ_H^c are larger than those of ρ_Q^c in some cases, meaning that first-order phase transitions do not appear in $\Delta_P = 0$ limits.

The values of ρ_E are densities at crossing points of energy densities $\epsilon_H(\rho)$ and $\epsilon_Q(\rho)$. In the case of H2+Q1e (H2+Q2e), the value of ρ_E is between (smaller than) ρ_H^c and ρ_Q^c.

In Fig. 8, pressures are given as a function of energy density ϵ in the transition region. The short-dashed curve is obtained by the H-EoS for H2 and the solid curve is by the Q-EoS for Q2. The bold solid curve is pressure in the interpolated region.

TABLE VI. Critical densities (fm^{-3}) of phase transitions: ρ_H and ρ_Q are densities at matching points in phase transitions from the hadronic phases for H1, H2, and H3 to the quark-matter phases for Q0, Q1, Q2, Q1e, and Q2e. ρ_H^c and ρ_Q^c are critical densities for the Maxwell construction defined by $P_H(\rho_H^c) = P_Q(\rho_Q^c) = P_c$. Values of ρ_E are densities at crossing points of energy densities $\epsilon_H(\rho)$ and $\epsilon_Q(\rho)$. There is no crossing point in the case of H1+Q2.

	ρ_H	ρ_Q	ρ_H^c	ρ_Q^c	ρ_E
H1+Q0	0.566	0.904	0.661	0.673	0.784
H1+Q1	0.490	0.703	0.574	0.544	0.918
H1+Q2	0.407	0.721	0.623	0.584	
H2+Q0	0.521	0.930	0.664	0.694	0.702
H2+Q1	0.446	0.712	0.573	0.561	0.753
H2+Q2	0.433	0.776	0.661	0.620	0.716
H2+Q1e	0.506	1.02	0.650	0.707	0.643
H2+Q2e	0.608	0.987	0.790	0.722	0.695
H3+Q0	0.482	0.922	0.616	0.689	0.659
H3+Q1	0.416	0.706	0.568	0.559	0.692
H3+Q2	0.407	0.772	0.608	0.612	0.660

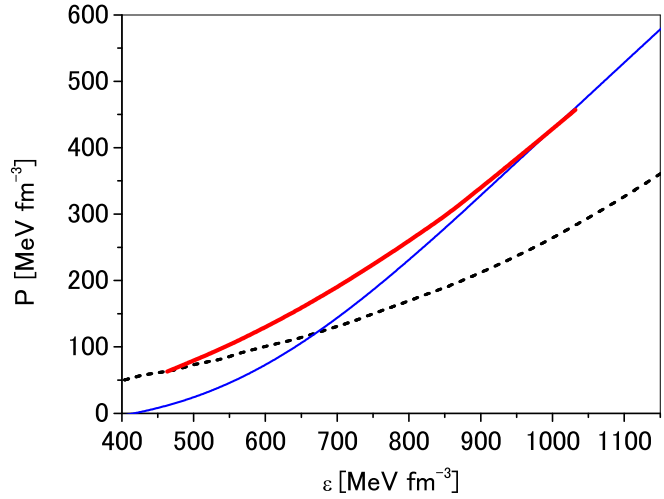

FIG. 8. Pressures as a function of as a function of the energy density ϵ in the region of phase transitions. The short dashed curves are obtained by the H-EoS for H2 and the solid curve is by the Q-EoS for Q2. The bold solid curve is the interpolated ones in the mixed phase.

It is worthwhile to point out that our hybrid-EoSs are consistent with the picture of hadron-quark continuity [17,18]. In these references, the interpolated pressures are given in the density region of $2 < \rho_B/\rho_0 <$ (4–7), where quark degrees of freedom gradually emerge. Correspondingly, our mixed phases are given in the region of (2.4–3.3) $< \rho_B/\rho_0 <$ (4.1–6.0), as found in Table VI.

Let us demonstrate that the Maxwell construction appears in the the $\Delta_P = 0$ limit. In Fig. 9, we show pressure P as a function of density ρ_B in the case of using H2+Q1e, where the dashed (short dashed) curves are for the hadronic (quark) matter. The horizontal solid lines show the range of the

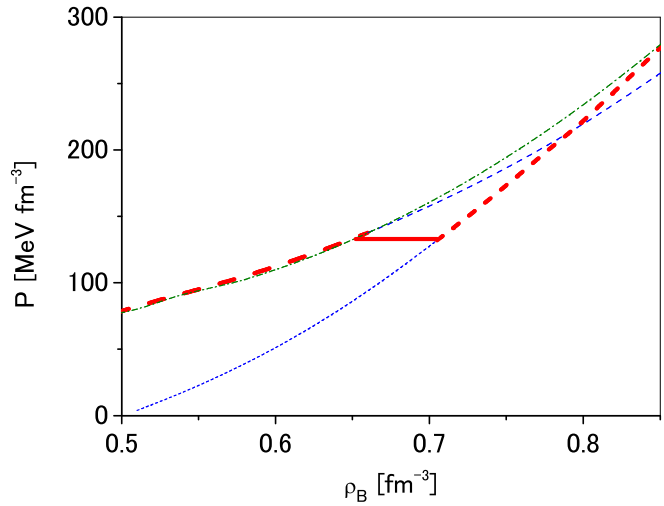

FIG. 9. Pressure P as a function of density ρ_B in the case of H2+Q1e, where the dashed (short dashed) curves are for hadronic (quark) matter. The horizontal solid line shows the range of the hadron-quark mixed phases in case of $\Delta_P = 0$. The dot-dashed curve is in the case of $\Delta_P = 0.07$.

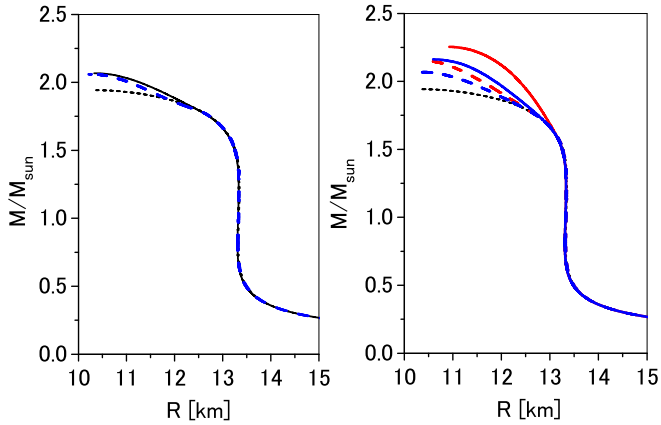

FIG. 10. Hybrid-star masses as a function of radius R, where the short dashed curves are obtained by the H-EoS for H2. In the left panel, the solid and dashed curves are obtained by H2+Q1e in cases of $\Delta_P = 0.07$ and $\Delta_P = 0$, respectively. In the right panel, the upper (lower) solid curves are obtained by H2+Q2 (H2+Q1), and the upper (lower) dashed curves are by H2+Q2e (H2+Q1e).

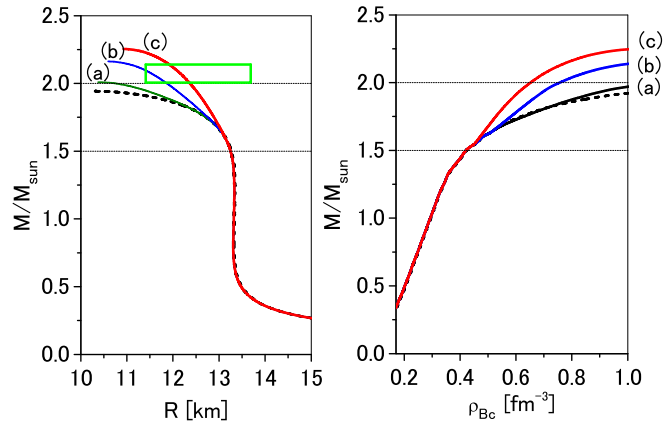

FIG. 11. Hybrid-star masses as a function of radius R (left panel) and central density ρ_{Bc} (right panel). The solid curves are obtained by the Q-EoSs for (a) Q0, (b) Q1, and (c) Q2. The short dashed curves are by the H-EoS for H2. The deviations from the latter to the formers are by phase transitions from hadronic matter to quark matter. The rectangle indicates the region of mass $2.072^{+0.067}_{-0.066}\mathrm{M}_\odot$ and radius $12.39^{+1.30}_{-0.98}$ km [22] for PSR J0740+6620.

hadron-quark mixed phase. It is well known that the Maxwell construction is specified by the horizontal line in the $P-\rho$ diagram, where the density values at ends of horizontal and vertical lines are given by ρ_H^c and ρ_Q^c. The difference of the curve for $\Delta_P = 0$ from the dot-dashed curve for $\Delta_P = 0.07$ is found to be small, the appearance of which is seen in the corresponding MR curves as shown later. Not only in the case of He+Q1e, there appear the similar curves specifying the Maxwell construction in the cases of $\rho_H^c < \rho_Q^c$ in Table VI.

Our hybrid-star EoS is composed of H-EoS and Q-EoS, being combined by the interpolation formula including the parameter Δ_P. The MR relations of hybrid stars can be obtained by solving the Tolmann-Oppenheimer-Volkoff (TOV) equation, where our hybrid EoSs are connected smoothly to the crust EoS [35,36] in the low-density side.

In Fig. 10, hybrid-star masses are shown as a function of radius R in the cases of using Q1e or Q2e (Q1 or Q2), where the short dashed curves are obtained by the H-EoS for H2.

In the left panel, the solid and dashed curves are obtained by H2+Q1e in cases of $\Delta_P = 0.07$ and $\Delta_P = 0$ (Maxwell construction), respectively. The slight reduction of the latter compared to the former is due to the difference between the $\Delta_P = 0.07$ and $\Delta_P = 0$ curves in in Fig. 9.

In the right panel, the upper (lower) solid curves are obtained by H2+Q2 (H2+Q1) in the case of $\Delta_P = 0.07$, and the upper (lower) dashed curves are by H2+Q2e (H2+Q1e). The maximum masses are $2.15M_\odot$ ($2.25M_\odot$) for H2+Q2e (H2+Q2), and $2.07M_\odot$ ($2.16M_\odot$) for H2+Q1e (H2+Q1). The quark-phase onset values of the central baryon densities are 0.54 fm^{-3} (0.48 fm^{-3}) in the case of H2+Q1e (H2+Q1), and 0.65 fm^{-3} (0.46 fm^{-3}) in the case of H2+Q2e (H2+Q2). Thus, Q2e (Q1e) leads to the larger onset density and the smaller maximum mass than Q2 (Q1): It is a general trend that maximum masses become smaller as onset densities of quark phases become larger.

In our approach, there is no clear criteria to decide which of Q2 (Q1) and Q2e (Q1e) is more appropriate. In the following section, we use Q1 and Q2 because they seem to be more suitable than Q1e and Q2e in the light of the recent observations for the maximum masses.

C. *MR* diagrams of hybrid stars

In Fig. 11, hybrid-star masses are given as a function of radius R (left panel) and central baryon density ρ_{Bc} (right panel). The curves obtained by the Q-EoSs for [Fig. 11(a)] Q0, [Fig. 11(b)] Q1, and [Fig. 11(c)] Q2 are given by solid curves, and those by the H-EoS for H2 are given by the short dashed curves. The former curves are connected from the latter curves by the hadron-quark phase transitions. The maximum masses for [Fig. 11(b)] Q1 and [Fig. 11(c)] Q2 are over $2M_\odot$ substantially. It is noted that the Q-EoS for [Fig. 11(a)] Q0 derived from V_{EME} is still stiff enough to reach $2M_\odot$ without help of the repulsive contributions of V_{OGE} and V_{MPP}. This repulsive components in V_{EME} come from vector-meson and pomeron exchanges between quarks. The rectangle in the left panel indicates the region of mass $2.072^{+0.067}_{-0.066}\mathrm{M}_\odot$ and radius $12.39^{+1.30}_{-0.98}$ km [22] for the most massive neutron star PSR J0740+6620. The MR curves for Q1 and Q2 are found to pass through this rectangle.

In the left panel of Fig. 12, hybrid-star masses are drawn as a function of radius R, where the Q-EoSs for Q2 and H-EoSs for [Fig. 12(a)] H1, [Fig. 12(b)] H2, and [Fig. 12(c)] H3 are used. Short dashed, long dashed, and dot-dashed curves are obtained with H-EoSs for H1, H2, and H3, respectively. Solid curves show deviations by transitions from hadronic-matter to quark-matter phases. The maximum masses in the figures are as follows: In the cases of H-EoSs, they are $1.82M_\odot$ (H1), $1.94M_\odot$ (H2), and $2.07M_\odot$ (H3). In the cases of including hadron-quark transitions, they are $2.25M_\odot$ (H1+Q2), $2.25M_\odot$ (H2+Q2), and $2.28M_\odot$ (H3+Q2). The maximum masses are noted to be determined by the Q-EoSs, being larger than those given by the H-EoSs. The rectangle in the left panel is the

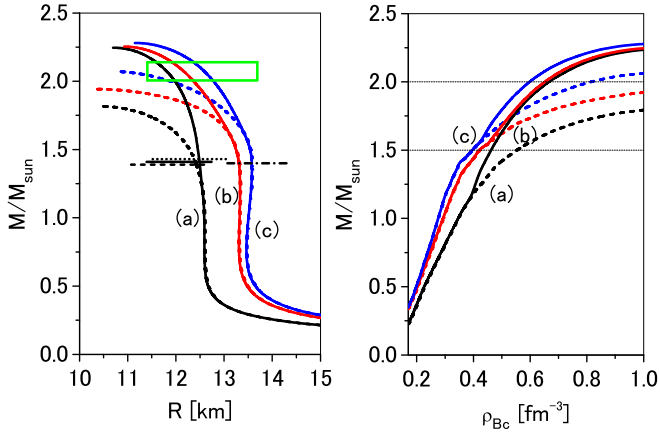

FIG. 12. Hybrid-star masses as a function of radius R (left panel) and central density ρ_{Bc} (right panel), where the Q-EoS for Q2 is used. Short dashed, long dashed, and dot-dashed curves are obtained with H-EoSs for (a) H1, (b) H2, and (c) H3, respectively. Solid curves show the deviations by transitions from hadronic-matter to quark-matter phases. In the left panel, the rectangle indicates the region of mass $2.072^{+0.067}_{-0.066}\mathrm{M}_\odot$ and radius $12.39^{+1.30}_{-0.98}$ km [22]. Dotted and solid line segments indicate $R_{1.4M_\odot} = 12.33^{+0.76}_{-0.81}$ km (PP model) and $R_{1.4M_\odot} = 12.18^{+0.56}_{-0.79}$ km (CS model) [24], and dashed and dot-dashed ones indicate $R_{1.4M_\odot} = 11.94^{+0.76}_{-0.87}$ km [25] and $R_{1.4M_\odot} = 13.80 \pm 0.47$ km [26], respectively.

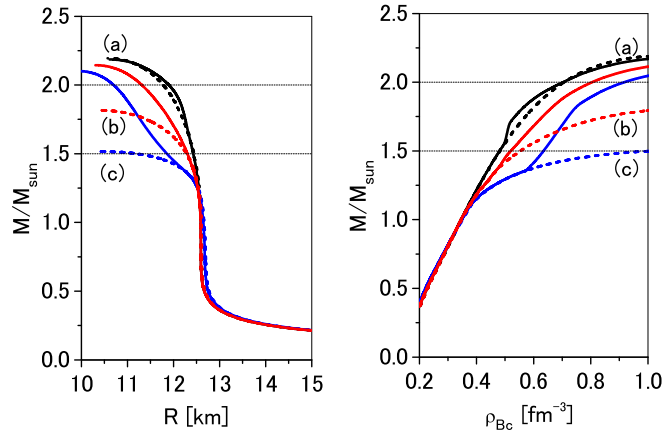

FIG. 13. Hybrid-star masses are given as a function of radius R (left panel), and as a function of central density ρ_{Bc} (right panel). The top dashed curve (a) is obtained from the H-EoS for H0 without hyperons. The middle dashed curve (b) is from the H-EoS for H1. The bottom dashed curve (c) is from the H-EoS for H1′ including hyperons, in which the MPP repulsions work only among nucleons. The solid curves show the deviations by transitions from hadronic phase to quark-matter phase for Q1.

same as that in Fig. 11, indicating the mass-radius region obtained from the observation [22]. The MR curves for the Q-EoSs pass through the rectangle, though those for the H-EoSs (dashed curves) are below this rectangle.

The radii R at $1.4M_\odot$ ($R_{1.4M_\odot}$) are given as follows: The values of $R_{1.4M_\odot}$ are 12.5 km (H1+Q2), 13.3 km (H2+Q2), and 13.6 km (H3+Q2), being obtained in the cases of including hadron-quark transitions. Similar values are obtained by using H-EoSs only, which means that the values of $R_{1.4M_\odot}$ are determined by H-EoSs. In the figure, dotted and solid line segments indicate $R_{1.4M_\odot} = 12.33^{+0.76}_{-0.81}$ km (PP model) and $R_{1.4M_\odot} = 12.18^{+0.56}_{-0.79}$ km (CS model) [24], and dashed and dot-dashed ones indicate $R_{1.4M_\odot} = 11.94^{+0.76}_{-0.87}$ km [25] and $R_{1.4M_\odot} = 13.80 \pm 0.47$ km [26], respectively. The former three line segments (dotted, solid, and dashed lines) are similar with each other, and the MR curve for H1 intersects them. On the other hand, the MR curves for H2 and H3 intersect the dot-dashed line, but do not intersect the other three lines. In the present stage of the observations for radii of neutron stars, it is difficult to determine which one of H1, H2, and H3 leads to the most reasonable EoS.

In the right panel of Fig. 12, hybrid-star masses are drawn as a function of central baryon density ρ_{Bc}, where the Q-EoS for Q2 is used. Short dashed, long dashed, and dot-dashed curves are obtained with H-EoSs for H1, H2, and H3, respectively. Solid curves show the deviations by transitions from hadronic-matter to quark-matter phases. In the cases of including hadron-quark transitions, the onset values of ρ_{Bc} for quark phases are 0.40 fm^{-3} (H1+Q2), 0.46 fm^{-3} (H2+Q2), and 0.43 fm^{-3} (H3+Q2).

It is useful to compare our results for MR diagrams with those in Ref. [14], because we employ the method in this reference for the hadron-quark phase transitions. Though their quark-matter EoS is based on the nonlocal Nambu-Jona-Lasinio (nlNJL) model, unlike ours, it is found that the quark-phase regions of the MR curves in Fig. 4 of Ref. [14] are similar to ours qualitatively. In particular, maximum masses of $2M_\odot$ are reproduced well; namely the Q-EoSs are stiff similarly here and in Ref. [14]. However, the hadronic-matter regions are different from each other, since softer H-EoSs are used in Ref. [14] than here.

As stated before, the hyperon mixing results in remarkable softening of the EoS. In order to avoid this "hyperon puzzle," the universal repulsions modeled as MPP are included in our derivations of our H-EoSs. Here, let us try to use the H-EoS for H1′ in which the MPP repulsions work only among nucleons. The BB interaction used in Ref. [14] is of this type. In Fig. 13, hybrid-star masses are given as a function of radius R (left panel) and of central density ρ_{Bc} (right panel). The top dashed curve [Fig. 13(a)] is obtained from the H-EoS for H0 without hyperons. The middle dashed curve [Fig. 13(b)] is from the H-EoS for H1. The bottom dashed curve [Fig. 13(c)] is from the H-EoS for H1′ including hyperons, in which the MPP repulsions work only among nucleons. The solid curves show the deviations by transitions from hadronic phase to quark-matter phase for Q1. It should be noted that the large difference from the top dashed curve to the bottom dashed curve demonstrates the softening of the EoS by hyperon mixing. Then, the solid curves show the deviations by transitions from hadronic phases to quark-matter phases for Q1. The lowering of the maximum mass by the EoS softening turns out to be recovered by the transition to the quark-matter phase given by the stiff EoS. It is interested that the curves for H0+Q1 are similar to those for H0. The basic feature of the MR curve for H1′+Q1 is similar to those of the curves in Ref. [14].

Our MR diagrams of hybrid stars are derived from H-EoSs for BB interactions (H1, H2, H3) and Q-EoSs for QQ

TABLE VII. Maximum masses $M_{\max}$ and radii $R_{M_{\max}}$, radii at $1.4M_\odot$ $R_{1.4M_\odot}$, dimensionless tidal deformability at $1.4M_\odot$ $\Lambda_{1.4M_\odot}$

	$M_{\max}/M_\odot$	$R_{M_{\max}}$ (km)	$R_{1.4M_\odot}$ (km)	$\Lambda_{1.4M_\odot}$
H1	1.82	10.4	12.4	422
H1+Q0	1.99	10.0	12.4	422
H1+Q1	2.14	10.3	12.4	422
H1+Q2	2.25	10.7	12.5	422
H1′	1.52	10.4	12.1	334
H1′+Q1	2.10	10.0	12.2	337
H2	1.94	10.3	13.3	671
H2+Q0	2.01	10.4	13.3	671
H2+Q1	2.16	10.6	13.3	671
H2+Q2	2.25	10.9	13.3	671
H3	2.07	10.7	13.6	771
H3+Q0	2.04	10.7	13.6	771
H3+Q1	2.18	10.8	13.6	771
H3+Q2	2.28	11.2	13.6	771

interactions (Q0, Q1, Q2): There are nine combinations of H-EoSs and Q-EoSs, among which some combinations are used in the above results. In Table VII, features of the obtained MR diagrams in all combinations of (H1, H2, H3) and (Q0, Q1, Q2) are demonstrated by showing the calculated values of maximum masses $M_{\max}$ and radii $R_{M_{\max}}$, and radii at $1.4M_\odot$ ($R_{1.4M_\odot}$). For comparison, those for H1′ and H1′+Q1 are added. Here, the important features are as follows: (1) In all cases, the Q-EoSs combined with the H-EoSs are stiff enough to reproduce maximum masses over $2M_\odot$. (2) The values of $R_{1.4M_\odot}$ are specified by the H-EoSs.

Another constraint for the EoS is given by the tidal deformability, being the induced quadruple polarizability. The dimensionless tidal deformability Λ is defined as $\Lambda = (2/3)k_2(c^2R/GM)^5$ [37], where c is the speed of light, R and M are radius and mass of a neutron star, and G is the gravitational constant. k_2 is the tidal Love number describing the response of each star to the external disturbance. The binary neutron star merger GW170817 give the upper limit on the tidal deformability of a neutron star with mass $1.4M_\odot$: $\Lambda_{1.4M_\odot} \leqslant 800$ [38]. Table VII gives the calculated values of $\Lambda_{1.4M_\odot}$ for our EoSs, where all values are less than the upper limit of 800. It should be noted that the values of $\Lambda_{1.4M_\odot}$ are determined by the H-EoSs, even if the Q-EoSs are combined with them.

V. CONCLUSION

The EoSs and MR diagrams of hybrid stars are obtained on the basis of our QQ interaction model composed of the extended meson exchange potential ($V_{\rm EME}$), the multipomeron exchange potential ($V_{\rm MPP}$), the instanton exchange potential ($V_{\rm INS}$), and the one gluon exchange potential ($V_{\rm OGE}$), whose strengths are determined on the basis of terrestrial data with no *ad hoc* parameter to stiffen EoSs. The repulsive nature of our QQ interaction in high-density region are basically given by $V_{\rm EME}$ including strongly repulsive components owing to vector-meson and pomeron exchanges. Additional repulsions (attractions) are given by $V_{\rm MPP}$ and $V_{\rm OGE}$ ($V_{\rm INS}$). The resultant repulsions included in our QQ interaction are so strong that the quark-matter EoSs become stiff enough to give maximum masses of hybrid stars over $2M_\odot$.

Hadronic-matter EoSs (H-EoS) and quark-matter EoSs (Q-EoS) are derived in the same framework based on the BBG theory. In quark matter, density-dependent quark masses are introduced phenomenologically, playing a decisive role in the occurrence of phase transition. Parameters of density dependences are taken so that hadron-quark phase transitions are able to occur at reasonable density region owing to the reduction of the quark masses and chemical potentials in quark matter. Our resulting density dependence of effective quark mass is similar to the Brown-Rho scaling.

Our H-EoSs are still not stiff enough to give maximum masses of neutron stars over $2M_\odot$ due to the softening by hyperon mixing, although the stiffness is recovered substantially by universal many-body repulsions. In the case of using our QQ interaction model, the Q-EoSs are stiffer than the H-EoSs and MR curves of hybrid stars shift above those of stars with hadronic phases only. The maximum masses of the formers including quark phases become larger than those of the latter, and MR curves are characterized by Q-EoSs in the mass region higher than about $1.5M_\odot$. Our Q-EoSs for Q1 and Q2 are stiff enough to give a maximum mass over $2M_\odot$. The derived mass and radius are consistent with the recent measurement for the most massive neutron star PSR J0740+6620, obtained by the combining analysis for the NICER and the other multimessenger data.

In our approach, star radii $R_{1.4M_\odot}$ given by hadronic-matter EoSs do not change by the hadron-quark phase transitions; namely they are determined by H-EoSs regardless of Q-EoSs. There are three estimates of $R_{1.4M_\odot}$ based on the NICER measurements and the other multimessenger data. Two of them give $R_{1.4M_\odot} = 11.1$–13.1 km, and the other $R_{1.4M_\odot} =$ 13.1–14.4 km. Our H-EoS for H1 (H2 or H3) is consistent with the former (latter).

Our H-EoSs and Q-EoSs lead to MR diagrams of hybrid stars consistent with the recent observations for masses and radii.

ACKNOWLEDGMENTS

The authors would like to thank D. Blaschke for valuable comments and fruitful discussions. This work was supported by Japan Society for the Promotion of Science (Grants No. 20K03951 and No. 20H04742).

[1] P. B. Demorest, T. Pennucci, S. M. Ransom, M. S. E. Roberts, and J. W. Hessels, Nature (London) **467**, 1081 (2010).

[2] J. Antoniadis, P. C. Feire, N. Wex, T. M. Tauns, R. S. Lynch, M. H. van Kerkwijk, M. Kramer, C. Bassa, V. S. Dhillon, T. Dnebe *et al.*, Science **340**, 6131 (2013).

[3] H. T. Cromartie, E. Fonceca, S. M. Ransom, P. B. Demorest, Z. Arzoumanian, H. Blumer, P. R. Brook, M. E. DeCesar, T. Dolch, J. A. Ellis *et al.*, Nat. Astron. **4**, 72 (2020).
[4] A. Akmal, V. R. Pandharipande, and D. G. Ravenhall, Phys. Rev. C **58**, 1804 (1998).
[5] S. Nishizaki, Y. Yamamoto, and T. Takatsuka, Prog. Theor. Phys. **105**, 607 (2001); **108**, 703 (2002).
[6] Y. Yamamoto, T. Furumoto, N. Yasutake, and T. A. Rijken, Phys. Rev. C **90**, 045805 (2014).
[7] Y. Yamamoto, T. Furumoto, N. Yasutake, and T. A. Rijken, Eur. Phys. J. A **52**, 19 (2016).
[8] Y. Yamamoto, H. Togashi, T. Tamagawa, T. Furumoto, N. Yasutake, and T. A. Rijken, Phys. Rev. C **96**, 065804 (2017).
[9] M. M. Nagels, T. A. Rijken, and Y. Yamamoto, Phys. Rev. C **99**, 044002 (2019); **99**, 044003 (2019).
[10] K. Schertler, S. Leupold, and J. Schaffner-Bielich, Phys. Rev. C **60**, 025801 (1999).
[11] M. Baldo, G. F. Burgio, and H.-J. Schulze, *Superdense QCD Matter and Compact Stars*, NATO Science Series 2: Mathematics, Physics, and Chemistry Vol. 197, edited by D. Blaschke and D. Sedrakian (Springer, Dordrecht, 2006).
[12] R. Lastowiecki, D. Blaschke, H. Grigorian, and S. Typel, Acta Phys. Pol. B **5**, 535 (2012).
[13] M. Shahrbaf, D. Blaschke, A. G. Grunfeld, and H. R. Moshfegh, Phys. Rev. C **101**, 025807 (2020).
[14] M. Shahrbaf, D. Blaschke, and S. Khanmohamadi, J. Phys. G: Nucl. Part. Phys. **47**, 115201 (2020).
[15] K. Maslov, N. Yasutake, D. Blaschke, A. Ayriyan, H. Grigorian, T. Maruyama, T. Tatsumi, and D. N. Voskresensky, Phys. Rev. C **100**, 025802 (2019).
[16] C.-J. Xia, T. Maruyama, N. Yasutake, and T. Tatsumi, Phys. Rev. D **99**, 103017 (2019).
[17] T. Kojo, P. D. Powell, Y. Song, and G. Baym, Phys. Rev. D **91**, 045003 (2015).
[18] G. Baym, T. Hatsuda, T. Kojo, T. D. Powell, Y. Song, and T. Takatsuka, Rept. Prog. Phys. **81**, 056902 (2018).
[19] K. Otto, M. Oertel, and B.-J. Schaefer, Phys. Rev. D **101**, 103021 (2020).
[20] T. Kunihiro, Phys. Lett. B **271**, 395 (1991).
[21] T. A. Rijken and Y. Yamamoto, Extended-soft-core quark-quark model constituent quark meson-exchange interactions, http://nn-online.org/eprints/pdf/20.06.pdf.
[22] T. E. Riley, A. L. Watts, P. S. Ray, S. Bogdanov, S. Guillot, S. M. Morsink, A. V. Bilous, Z. Arzoumanian, D. Choudhury, J. S. Deneva *et al.*, Astrophys. J. Lett. **918**, L27 (2021).
[23] M. C. Miller, F. K. Lamb, A. J. Dittmann, S. Bogdanov, Z. Arzoumanian, K. C. Gendreau, S. Guillot, W. C. G. Ho, J. M. Lattimer, M. Loewenstein *et al.*, Astrophys. J. Lett. **918**, L28 (2021).
[24] G. Raaijmakers, S. K. Greif, K. Hebeler, T. Hinderer, S. Nissanke, A. Schwenk, T. E. Rilley, A. L. Watts, J. M. Lattimer, and W. C. G. Ho, Astrophys. J. Lett. **918** , L29 (2021).
[25] P. T. H. Pang, I. Tews, M. W. Coughlin, M. Bulla, C. Van Den Broeck, and T. Dietrich, ApJ **922**, 14 (2021).
[26] B. T. Reed, F. Fattoyev, C. J. Horowitz, and J. Piekarewicz, Phys. Rev. Lett. **126**, 172503 (2021).
[27] M. Hutter, Interaction in QCD, theory, and application of the instanton liquid model, Ph.D. thesis, University of Munich, Munich, Germany, 1995.
[28] D. Blaschke, H. Grigorian, and G. Röpke, Particles **3**, 477 (2020).
[29] G. E. Brown and M. Rho, Phys. Rev. Lett. **66**, 2720 (1991).
[30] K. Kashiwa, H. Kouno, T. Sakaguchi, M. Matsuzaki, and M. Yahiro, Phys. Lett. B **647**, 446 (2007).
[31] S. Benic, Eur. Phys. J. A **50**, 111 (2014).
[32] Y. Yamamoto, T. Motoba, and T. A. Rijken, Prog. Theor. Phys. Suppl. No. **185**, 72 (2010).
[33] V. Abgaryan, D. Alvarez-Cstillo, A. Ayriyan, D. Blaschke, and H. Grigorian, Universe **4**, 94 (2018).
[34] N. K. Glendenning, Phys. Rev. D **46**, 1274 (1992).
[35] G. Baym, A. Bethe, and C. Pethick, Nucl. Phys. A **175**, 225 (1971).
[36] G. Baym, C. J. Pethick, and P. Sutherland, Astrophys. J. **170**, 299 (1971).
[37] B. P. Abbott *et al.* (LIGO Scientific and Virgo Collaborations), Phys. Rev. Lett. **119**, 161101 (2017).
[38] J. Piekarewicz and F. J. Fattoyev, Phys. Rev. C **99**, 045802 (2019).